Intermetallics 164 (2024) 108083

Contents lists available at ScienceDirect

Intermetallics

journal homepage: www.elsevier.com/locate/intermet

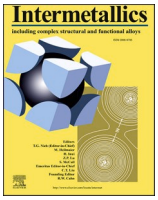

Hot deformation behavior of a Fe_3Al–Ta alloy in the B2-order regime

Aliakbar Emdadi [a,*], Michael Tovar [b], Angelika Jedynak [c], Sabine Weiß [a]

[a] Chair of Physical Metallurgy and Materials Technology, Brandenburg University of Technology Cottbus-Senftenberg, Konrad-Wachsmann-Allee 17, Cottbus 03046, Germany
[b] Helmholtz-Zentrum Berlin für Materialien und Energie GmbH, Hahn-Meitner-Platz 1, Berlin, 14109, Germany
[c] Chair of Hybrid Manufacturing, Brandenburg University of Technology Cottbus-Senftenberg, Konrad-Wachsmann-Allee 17, Cottbus 03046, Germany

ARTICLE INFO

Keywords:
A. Iron aluminides
Fe–25Al-1.5Ta alloy
B. Deformation map
Constitutive equation
C. Thermomechanical processing
D. microstructure
E. Dynamic materials modeling

ABSTRACT

In the present work, the hot deformation behavior and the corresponding microstructure evolution of an Fe–25Al-1.5Ta (at.%) alloy in the B2-phase field were investigated. Uniaxial compression tests were carried out in a strain rate range from 0.0013 s^{-1} to 1 s^{-1} and in a temperature range from 800 °C to 850 °C, where an ordered B2–FeAl matrix phase along with a C14 - $(Fe, Al)_2Ta$ Laves phase was confirmed by X-ray diffraction. A dynamic material model was applied to predict the safe and damaging processing windows. The underlying flow softening mechanisms were characterized using scanning electron microscopy and electron-backscatter diffraction. The flow stress-strain curves mostly showed a broad maximum followed by a slight decrease in stress until a steady stress was reached. The optimum processing window for the studied alloy was located at 850 °C/0.0013 s^{-1}, where the efficiency of power dissipation (η) and strain rate sensitivity (m) reached 50% and 0.25, respectively. The processing map also showed a domain of flow instability, resulting from cracking, in the range of lower temperatures and higher strain rates (800 °C/1 s^{-1}). The microstructural analyses confirmed a combination of dynamic recovery (DRV) and dynamic recrystallization (DRX) over the entire range of deformation conditions tested. The current study reveals a well-suited parameter range to achieve a high degree of hot deformability in Fe–Al alloys at significantly lower temperatures than those typically used. This may contribute to optimizing the thermomechanical processing of Fe–Al alloys and reducing energy consumption in industrial forging operations.

1. Introduction

Iron aluminides are Fe–Al alloys with 20–50 at.%[1]Al, in which the matrix consists of the disordered bcc (Fe, Al) solid solution (A2) or the ordered intermetallic phases FeAl (B2) and Fe_3Al ($D0_3$). They feature excellent oxidation resistance, about 30% lower density than commercial superalloys, low manufacturing costs, and can reduce the use of strategic elements such as Ni, Cr, and Mo in materials for structural applications [1]. Iron aluminide-based alloys may address a key challenge of the power generation industries to replace more creep-resistant and lightweight alloys for heavy and partly expensive advanced steels in ultra-supercritical steam turbines [1,2]. Nonetheless, low strength and creep resistance at temperatures above 600 °C have limited their potential application [1].

Iron aluminides based on Fe–25Al–2Ta strengthened with an incoherent intermetallic Laves phase revealed higher (creep) strengths at 650 °C than high-alloyed steels [3–5]. Steam turbine blades were successfully fabricated from Fe–25Al–2Ta alloys by industrial forging [6]. The addition of 2 at.% Ta to Fe_3Al-based alloys does not affect the excellent oxidation resistance of the alloy up to 800 °C [7].

At room temperature, the Fe_3Al binary alloy has an ordered $D0_3$ crystal structure, transforming into the ordered B2 structure at 546 °C (for the binary Fe-26 at.% Al alloy [8]). The B2 transforms into a disordered A2 structure at 829 °C. Further ternary ordering by Ta may lead to the formation of the $L2_1$ $TaFe_2Al$ Heusler phase (a ternary equivalent of $D0_3$ Fe_3Al) and the Laves phase, C14 - $(Fe, Al)_2Ta$ [9]. Thermo-Calc computations of an Fe–25Al-1.5Ta alloy indicated that the C14 Laves phase formed by the eutectic reaction L ↔ α-(Fe, Al) + C14 at around 1150 °C, remained stable to lower temperatures, around 570 °C, and transformed into the Heusler phase on further cooling [10–12].

Hot deformation behavior and microstructure evolution of Fe–25Al-1.5Ta alloys have been investigated in the temperature range of

* Corresponding author.
E-mail address: emdadi@b-tu.de (A. Emdadi).

[1] All compositions are given in the text in atomic percent unless otherwise stated.

https://doi.org/10.1016/j.intermet.2023.108083
Received 25 May 2023; Received in revised form 6 October 2023; Accepted 9 October 2023
Available online 27 October 2023
0966-9795/© 2023 The Authors. Published by Elsevier Ltd. This is an open access article under the CC BY license (http://creativecommons.org/licenses/by/4.0/).

900–1100 °C, where a disordered A2 α-(Fe, Al) solid solution phase is stable along with the C14 Laves phase [10,11,13]. The alloy shows a high degree of deformability and flow softening in the deformation range of 900–1100 °C/0.0013–1 s^{-1} in both spark plasma sintered and as-cast states. Laser powder bed fusion (L-PBF) additive manufacturing of Fe–25Al-1.5Ta alloys was also investigated [14–16], which could open up new possibilities to combine the beneficial properties of precipitation-strengthened Fe–Al–Ta iron aluminides with the geometric complexity of L-PBF to produce lightweight high-temperature resistant model alloys for turbine blades.

The deformation behavior and hot workability of Fe_3Al- and FeAl-based alloys have been investigated in the A2-phase field [11,17,18] and over a wide temperature range covering both A2-and B2-phase fields [19–21]. However, almost all of these studies lack the constitutive modeling of the hot deformation behavior and detailed characterization of the flow instability mechanism(s). The static recovery and recrystallization behaviors of particle-free and particle-containing Fe_3Al intermetallics during post-deformation annealing were studied in the B2 temperature range [22]. Nevertheless, the dynamic recovery and recrystallization behaviors of particle-containing Fe_3Al-based alloys in the B2-phase region have rarely been investigated. Therefore, the present study continues the authors' previous study and carries out a kinetic analysis of the deformation behavior coupled with hot workability evaluation in the temperature range of the ordered B2 phase in the Fe–25Al-1.5Ta alloy containing Laves phase precipitates at the deformation temperature.

From the point of view of sustainability and energy consumption in industrial forging, it is crucial to deform the material safely at the lowest possible temperatures. The possibility of deformation processing at low temperatures also reduces the problems associated with the oxidation of forging tools and dies, thus contributing to the long durability of dies. A possible challenge in deforming Fe_3Al-based alloys at lower temperatures could be the presence of the ordered B2–FeAl phase at temperatures below ~850 °C [23,24]. The B2 phase is more difficult to deform than the A2 due to the low mobility of superdislocations and the difficulty of cross slip. Furthermore, deformation mechanisms based on self-diffusion are also hindered by the ordering effects in B2 [25]. As a result, it is necessary to investigate the thermomechanical treatment of the alloy in the B2-phase field to identify the optimum processing window where the material can be safely deformed. This knowledge is vital, but the literature is insufficient considering the attempts currently being made to (re)evaluate the use of advanced iron aluminides in fossil-fuel power plants, as well as in the automotive, aviation, and marine industries [26].

The aim of the present study is, therefore, to investigate the deformability of the Fe–25Al-1.5Ta alloy at low temperatures of 800–850 °C where the ordered B2 and C14-Laves phases coexist. A suitable processing window for safe deformation of the alloy in the (B2 + C14)-phase field will be determined by the dynamic materials model (DMM). In particular, the dependence of flow stress on temperature and strain rate will be studied, and hot workability will be assessed using the concept of processing maps. The microstructure evolution during hot deformation will be analyzed to identify flow softening and flow instability/damage mechanisms at different deformation conditions.

2. Materials and methods

2.1. Specimen manufacturing

The pre-alloyed, gas-atomized Fe–25Al-1.5Ta (at.%) powder was consolidated using the field-assisted sintering technology (FAST), also known as spark plasma sintering (SPS). The sintering process was carried out in a vacuum at a temperature of 1200 °C for a holding time of 5 min and under a compaction force of 35 kN. The processing and initial powder characterization details can be found in Ref. [11].

2.2. Phase identification

The phase identification at 800 °C was performed by a Bruker D8 ADVANCE X-ray diffractometer (Bruker, Billerica, MA, USA) using Cu-$K_{\alpha 1}$ radiation ($\lambda = 0.15406$ nm) under a vacuum of 9.4×10^{-3} mbar within the 2θ range of 15–70° and a step size of 0.05°.

2.3. Hot compression tests

Cylindrical specimens with a diameter of 5 mm and a height of 8 mm were cut from the SPSed ingot using an electric discharge wire-cutting machine. Lab-scale isothermal compression tests were conducted on a DIL805A/D/T deformation dilatometer under Ar atmosphere. The specimens were heated to the deformation temperature with an induction heating system at a rate of 10 K/s and kept isothermal for 3 min to homogenize the temperature within the specimens before compression. The specimens were compressed in the temperature range between 800 °C and 850 °C, where the ordered B2 and C14 Laves phases are stable (the SPSed Fe–25Al-1.5Ta alloy showed a B2-to-A2 order-disorder transition at around 875 °C [11]) with strain rates from 0.0013 s^{-1} to 1 s^{-1} up to a true strain of 0.8. The deformed specimens were cooled immediately after deformation to preserve the high-temperature microstructures.

2.4. Microstructure characterization

A high-resolution electron backscatter diffraction system (EBSD - Oxford Instruments Aztec system, UK) operating in a scanning electron microscope (SEM - Zeiss Gemini 1550) was employed to obtain microstructural and crystallographic information. The individual grains were outlined with a threshold angle of 15° using the MTEX toolbox in MATLAB. Low- and high-angle grain boundaries (LAGBs/HAGBs) were defined with misorientations (θ) of 3–15° and more than 15°, respectively. All observations were carried out in the center of the deformed specimens.

2.5. Differential scanning calorimetry

Differential scanning calorimetry (DSC) was performed using a DSC 404 F3 Pegasus® (NETZSCH) between 400 and 1200 °C with a heating rate of 20 K/min to identify the order-disorder transition temperature of the B2 to the A2 structure.

2.6. Strain rate sensitivity map

The relationship between the true stress and the true strain rate in the logarithmic scale can be well expressed by a 3-order polynomial fit using the following equation:

$$log\ \sigma = a + b log\dot{\varepsilon} + c(log\dot{\varepsilon})^2 + d(log\dot{\varepsilon})^3 \quad (1)$$

where a, b, c, and d are material parameters depending on the temperature. By forming partial differentials on both sides of Equation (1), the strain rate sensitivity, m, can be formulated by:

$$m = \frac{\partial(log\ \sigma)}{\partial(log\dot{\varepsilon})} = b + 2c\ log\dot{\varepsilon} + 3d\ (\log\dot{\varepsilon})^2 \quad (2)$$

The 3D variation of m as a function of T and $\dot{\varepsilon}$ is plotted, and the possible correlation between the variation of m and the microstructure evolution during hot deformation is discussed.

2.7. Dynamic materials model

The concept of processing maps, based on the principles of the dynamic materials model (DMM), was first proposed by Prasad [27] to model the hot forging behavior of a Ti-6242 alloy. Strain rate sensitivity

(m), activation energy (Q), the efficiency of power dissipation (η), and instability maps are used to evaluate the hot workability of the material in question. DMM gives a physical interpretation of the strain rate sensitivity of flow stress, m, as a power-partitioning factor between heat generation during plastic flow and microstructural change.

A processing map can predict either 'safe' or 'unsafe' hot deformation domains for a given material. Dynamic recovery (DRV), dynamic recrystallization (DRX), and superplasticity are the safe mechanisms. In contrast, flow localization, adiabatic heating, dynamic strain aging, void formation, and cracking are damage mechanisms leading to flow instability [28,29]. A processing map is built by superimposing a power dissipation map and an instability map. At a given temperature in the hot working regime, the externally applied power is consumed via two major paths: heat generation due to plastic flow and dissipation by microstructural changes. The instantaneously dissipated total power is determined by the following:

$$P = \int_0^{\dot{\bar{\varepsilon}}} \bar{\sigma}.d\dot{\bar{\varepsilon}} + \int_0^{\bar{\sigma}} \dot{\bar{\varepsilon}}.\, d\bar{\sigma} = G + J \tag{3}$$

where $\bar{\sigma}$ and $\dot{\bar{\varepsilon}}$ are the effective stress and the effective strain rate, respectively. The first and second integrals are called G (content) and J (co-content) and represent the power dissipation through plastic deformation and microstructural dissipation, respectively. The relative partitioning of power between heat generation and microstructural transitions is defined by the strain rate sensitivity (of flow stress), m, as follows:

$$m = \frac{dJ}{dG} = \frac{\dot{\bar{\varepsilon}}\, d\bar{\sigma}}{\bar{\sigma} d\dot{\bar{\varepsilon}}} = \frac{d\,(ln\bar{\sigma})}{d\,(ln\dot{\bar{\varepsilon}})} \tag{4}$$

The efficiency of power dissipation (η) with respect to a linear dissipator ($m = 1$) is defined by:

$$\frac{\Delta J/\Delta P}{(\Delta J/\Delta P)linear} = \frac{m/(m+1)}{1/2} = \frac{2m}{m+1} \equiv \eta \tag{5}$$

A power dissipation map displays the 3D variation of η as a function of temperature and strain rate.

Instability maps are developed based on a continuum instability criterion derived from the extremum principles of irreversible thermodynamics when applied to continuum mechanics of large plastic flow proposed by Ziegler [30]. The instability criterion is given by the dimensionless parameter ξ as follows:

$$\xi(\dot{\bar{\varepsilon}}) = \frac{\partial \ln\,(m/m+1)}{\partial ln\dot{\varepsilon}} + m \leq 0 \tag{6}$$

A flow instability map represents the variation of the dimensionless instability parameter, ξ, with deformation temperature and strain rate. The parameter ξ is calculated by substituting Equation (2) in Equation (6) as follows:

$$\xi(\dot{\varepsilon}) = \frac{2c + 6d\ log\dot{\varepsilon}}{m(m+1)\ ln\dot{\varepsilon}} + m \tag{7}$$

The temperature and strain rate regime with negative ξ values results in flow instability, which should be avoided during hot deformation operations. In contrast, the temperature and strain rate condition where the efficiency of power dissipation takes its maximum without flow instability is considered as the optimum processing window for hot working. Based on the results obtained from microstructural investigations, deformation mechanisms are characterized and correlated with different regions of processing maps.

3. Results

3.1. Phase constituents at deformation temperature

The differential scanning calorimetry (DSC) flow curve during heating is shown in Fig. 1(a), which indicates the B2-order to A2-disorder transition temperature at around 875 °C. The XRD pattern of the studied alloy at 800 °C shown in Fig. 1(b) also confirms a phase mixture of B2 and C14 in the material at a deformation temperature of 800 °C. Therefore, it is confirmed that the deformation in the selected temperature range of 800–850 °C was performed in a dual-phase field composed of B2 and C14 Laves phases. An earlier investigation revealed that the C14 precipitations mainly decorate the grain boundaries of the Fe–Al matrix [10,11].

3.2. Flow stress-strain behavior

Fig. 2 shows the true strain–true stress curves of the Fe–25Al-1.5Ta samples hot compressed to a true strain of 0.8 at different temperatures and strain rates. Deformation temperature and strain rate affect the flow stress behavior of the studied alloy. The flow stress decreases with decreasing strain rate and increasing temperature. In the case of a higher strain rate of 1 s^{-1}, the curves show a stress peak followed by a drop of stress, which is pretty similar to the typical curve for dynamic recrystallization (DRX) of FCC metals and alloys [31]. The flow curves at 0.0013 s^{-1}, 0.01 s^{-1}, and 0.1 s^{-1} show a broad flow stress peak followed by a slight decrease. This shape is typical for DRX in conventional BCC metals like αFe, where a pronounced stress drop in flow stress-strain curves was not observed despite the occurrence of DRX [32,33]. None of the curves shows the obviously flat shape typical of dynamic recovery (DRV).

3.3. Kinetic analysis of flow behavior and constitutive equation

A constitutive equation presents the functional dependence of flow stress on the hot deformation parameters, including strain, strain rate, and temperature. When a material undergoes deformation at elevated temperatures, the relationship between flow stress and processing parameters is generally expressed by the classical hyperbolic function proposed by Sellars and Tegart [34]:

$$\dot{\varepsilon} = A\ [\sinh\ (\alpha\sigma)]^n\ \exp\left(-\frac{Q}{RT}\right) \tag{8}$$

where $\dot{\varepsilon}$ is the strain rate (s^{-1}), σ the steady-state stress (MPa), Q the apparent activation energy of hot deformation (kJ.mol^{-1}), T the absolute deformation temperature (K), R the universal gas constant (8.314 J mol^{-1} K^{-1}), n the stress component, and A and α are material constants. By taking the natural logarithm from Equation (8), Q can be obtained by:

$$Q = R.\left(\frac{\partial ln\dot{\varepsilon}}{\partial ln[\sinh(\alpha\sigma)]}\right)_T.\left(\frac{\partial ln[\sinh(\alpha\sigma)]}{\partial(1/T)}\right)_{\dot{\varepsilon}} \tag{9}$$

The material constant α is given by:

$$\alpha = \frac{\beta}{n_1} = \frac{(\partial ln\dot{\varepsilon}/\partial\sigma)_T}{(\partial ln\dot{\varepsilon}/\partial ln\ \sigma)_T} \tag{10}$$

The relationships between σ, lnσ, and ln $\dot{\varepsilon}$ at a true strain of 0.8 are plotted in Fig. 3. The slope in the plots obtained by linear regression gave an average value of 6.27 for n_1 and 0.033 for β. Subsequently, the constant α is calculated as 0.005 according to Equation (10).

The plots for (ln $\dot{\varepsilon}$ - ln[sinh($\alpha\sigma$)]) and (ln[sinh($\alpha\sigma$)] - 1/T) at a true strain of 0.8 are plotted in Fig. 4(a) and (b). The obtained average slopes in the plots provide an average of 540 kJ mol^{-1} for Q at a strain of 0.8. This value is comparatively higher than that of Q obtained for the SPSed Fe–25Al-1.5Ta alloy in the disordered A2 regime (436 kJ mol^{-1} [11]), indicating that the ordered B2–FeAl is more resistant to deformation than the disordered A2.

In Table 1, the activation energies for hot deformation are compared for several iron aluminides.

A temperature-compensated strain rate, known as the Zener-Hollomon parameter (Z), is usually used to show the combined effect

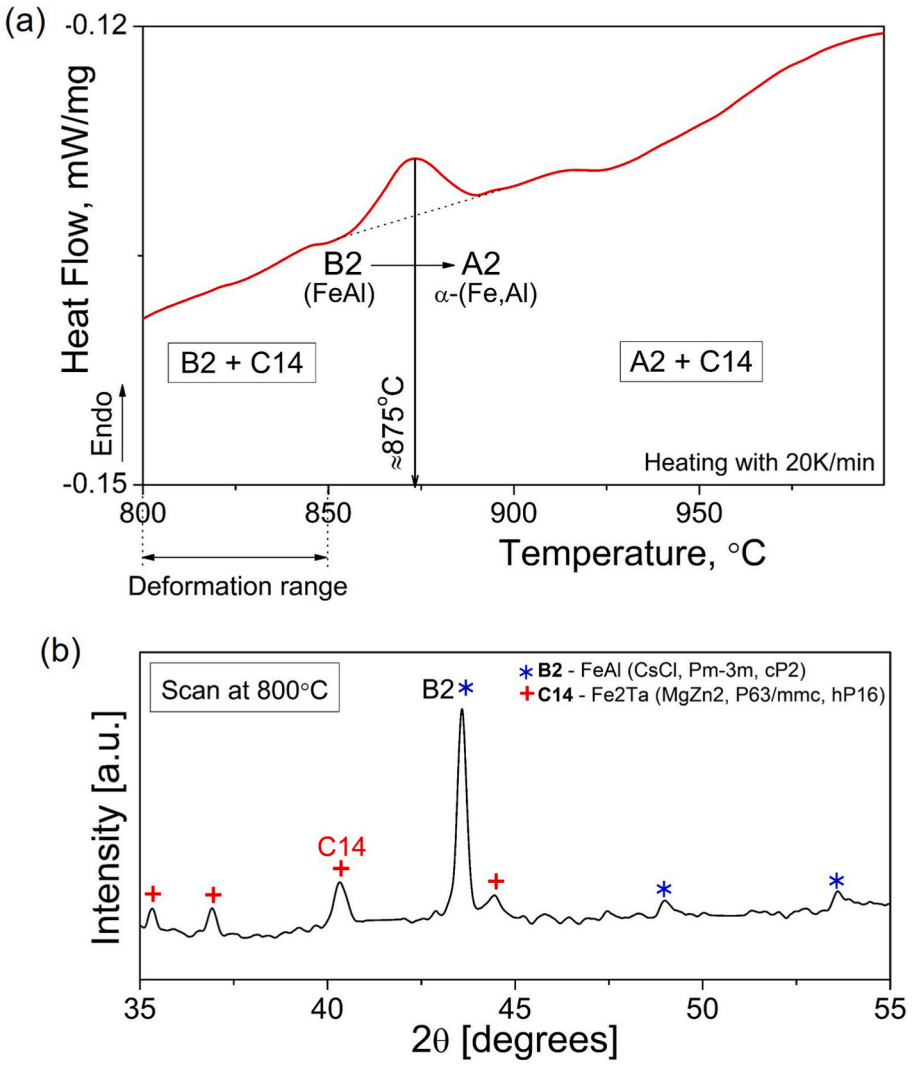

Fig. 1. DSC heat flow curve for a Fe–25Al-1.5Ta sample showing the order-disorder transition temperature at around 875 °C (a) and XRD pattern at 800 °C showing a dual-phase mixture of B2 and C14 Laves phase at the hot deformation temperature. The temperature range of hot deformation is indicated in (a).

of deformation temperature and strain rate on the deformation process. Z is given by:

$$Z = \dot{\varepsilon}\exp\left(Q/RT\right) = A[\sinh(\alpha\sigma)]^n \tag{11}$$

The obtained average Q value was used to calculate Z by Equation (11). In Fig. 4(c), the dependence of ln$Z$ on ln[sinh($\alpha\sigma$)] at a true strain of 0.8 was plotted. The stress peak is sensitive to the deformation variables, and the peak stress value is influenced by Z. By linear fitting, the constants of n and A in Equation (11) are calculated as 4.87 and 2.8×10^{32}, respectively. The constant α was already calculated as 0.005 by Equation (10). The constitutive equation for the hot deformation of the studied Fe–25Al-1.5Ta alloy associated with steady-state stress can be formulated as follows:

$$\sigma = \frac{1}{0.005}\, ln\left[\left(\frac{Z}{2.8\times10^{32}}\right)^{1/4.87} + \left(\left(\frac{Z}{2.8\times10^{32}}\right)^{2/4.87} + 1\right)^{1/2}\right] \tag{12}$$

3.4. Strain rate sensitivity map

A strain rate sensitivity (m) map for the SPSed Fe–25Al-1.5Ta alloy deformed in the (B2 + C14)-phase field at a true strain of 0.8 is displayed in Fig. 5. The values of m vary between 0.08 and 0.29 for the deformation conditions tested. Importantly, deformation at 800 °C/1 s^{-1} causes negative m values, as indicated by an arrow on the map. Negative m values correspond to flow instability mechanisms, including flow localization, shear band formation, dynamic strain aging, and cracking [28].

3.5. Processing map

A processing map is built by superimposing the power dissipation map and the instability map, which reveals windows representing various microstructural mechanisms and the constraints of flow instabilities. The optimum intrinsic workability of the material can be achieved using the processing windows that are safe processing domains with the most efficient power dissipation. The iso-contour processing map for the SPSed Fe–25Al-1.5Ta alloy deformed in the (B2 + C14)-phase-field for the maximum true strain of 0.8 is shown in Fig. 6. The processing map represents different regions; stable flow regions with high efficiency are highlighted in yellow and are denoted as D1 and D2, as well as a region with low efficiency, including flow instability shaded and denoted as D3. The flow instability predicted for the deformation conditions 800 °C/1s^{-1} resulted from a negative strain rate sensitivity (see Fig. 5). The possibility of safe deformation over almost all tested deformation conditions suggests high hot workability for the investigated Fe–25Al-1.5Ta alloy in the temperature range of 800–850 °C.

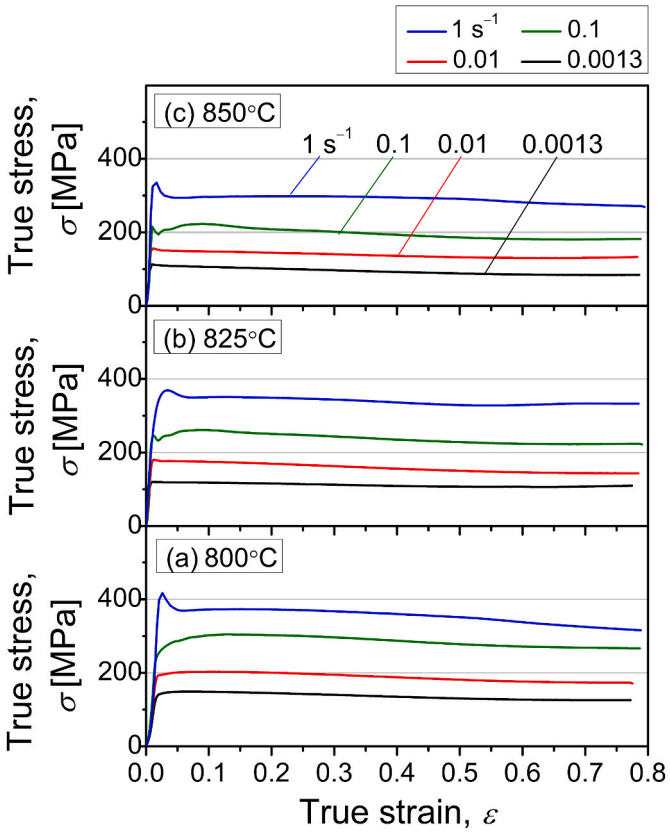

Fig. 2. True stress-strain flow curves for the SPSed Fe–25Al-1.5Ta alloy specimens hot compressed up to a true strain of 0.8 at 800 °C (a), 825 °C (b), and 850 °C (c) with different strain rates.

3.6. Characterization of the deformed specimens

The microstructures of the specimens deformed at different deformation conditions of the processing map are shown in Fig. 6. The specimens deformed with the higher strain rate of 1s^{-1} between 800 °C and 825 °C exhibit micro-cracks originating from the surfaces in contact with the deformation punches. In addition, the specimen compressed at 800 °C/1 s^{-1} revealed a longitudinal macro-crack expanding through its surface.

4. Discussion

The studied Fe–25Al-1.5Ta alloy exhibits a B2 (FeAl) → A2 (αFe) transformation at about 875 °C. The temperature range investigated for hot deformation behavior was from 800 to 850 °C in the (B2+C14)-phase field region. The B2 phase is more difficult to deform than the A2 due to the low mobility of superdislocations and the difficulty of cross-slip through the superlattice. Furthermore, deformation mechanisms based on self-diffusion are also impeded by the ordering effects in B2. It is well known that the grain boundary mobility is drastically reduced in the presence of order, which severely retards recrystallization [39]. Transmission electron microscopy observations in the deformed Fe_3Al-based alloys [22] indicated the rearrangement of dislocations and the formation of dislocation walls at the early stage of annealing within the B2-phase field region. At a later stage of annealing, the well-defined subgrains enclosed by low-angle boundaries were formed. In addition, a mechanism of grain boundary migration by bulging of the original grain boundaries was also frequently observed in Fe_3Al-based alloys at the early stage of annealing within the B2-phase filed region [22]. A similar effect of B2 on recrystallization was also observed in duplex (FCC + BCC/B2) high entropy alloys. It was reported that the significantly lower strain partitioning in the B2 phase coupled with its ordered structure would significantly reduce the driving force for recrystallization and promote recovery in duplex high entropy alloys [40–42].

Fig. 7 shows SEM backscatter electron images of longitudinal cross-sections of the Fe–25Al-1.5Ta specimens compressed up to a true strain of 0.8 at different temperatures and strain rates. The microstructure of

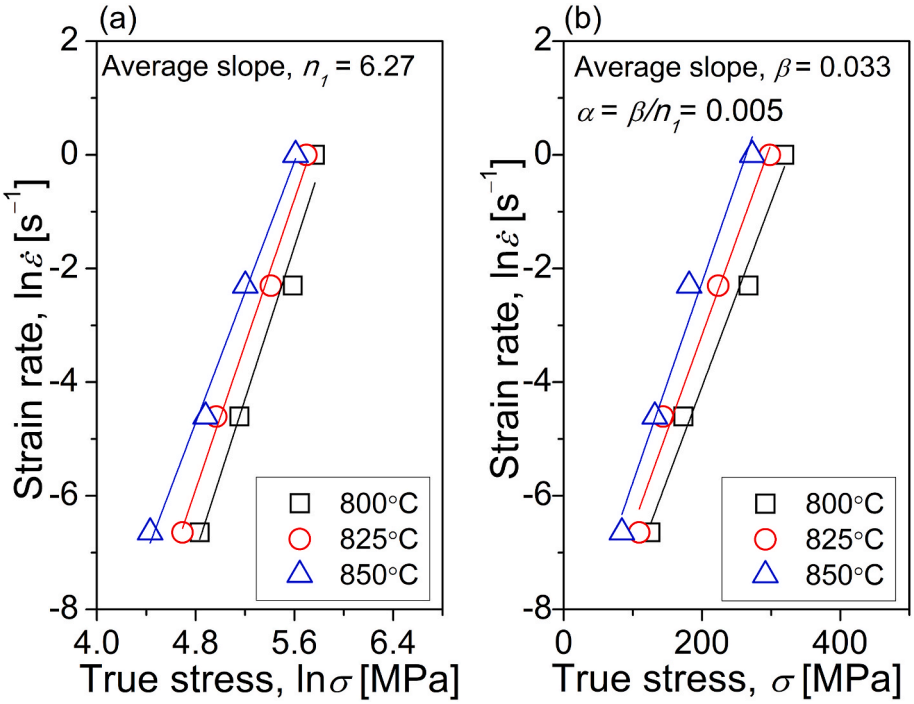

Fig. 3. Flow stress analysis for the Fe–25Al-1.5Ta alloy showing linear fit for the ln (strain rate) vs. ln (stress) (a) and ln (strain rate) vs. stress (b) obtained from the flow stress-strain curves at a strain of 0.8. The average slope values in (a) and (b) are the parameters n_1 and β, respectively, and β/n_1 gives α.

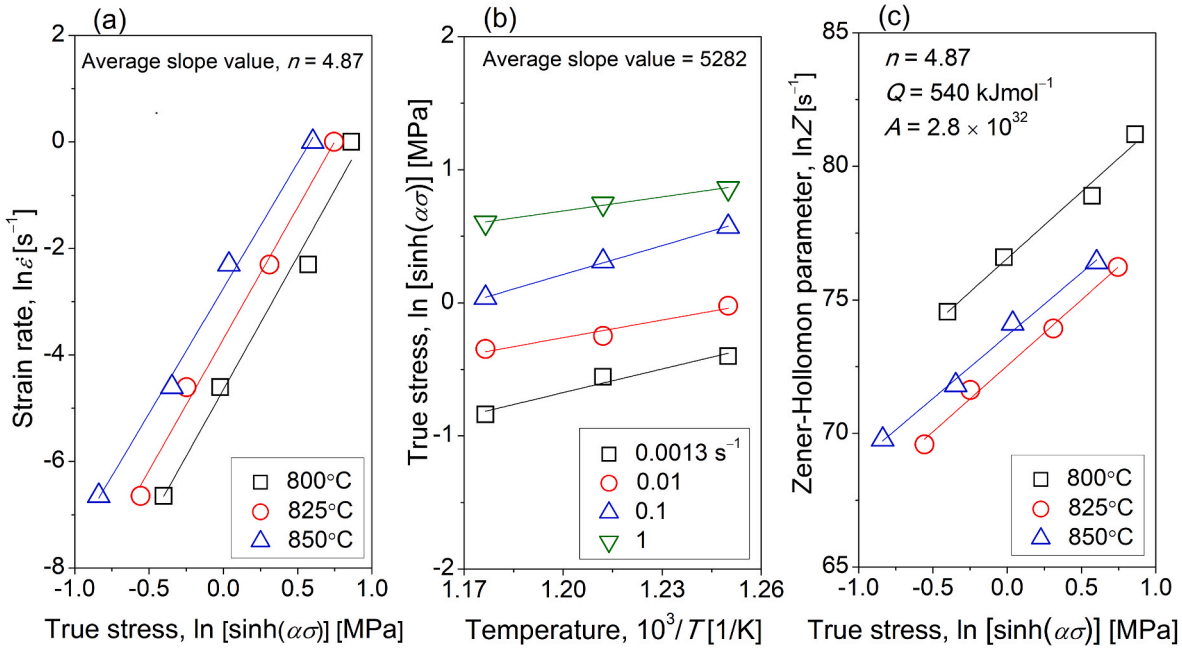

Fig. 4. Flow behavior kinetic analysis for the Fe–25Al-1.5Ta alloy showing linear fit for the ln $\dot{\varepsilon}$ *vs.* ln[sinh($\alpha\sigma$)] at different temperatures (a), ln[sinh($\alpha\sigma$)] *vs.* $1/T$ at different strain rates (b), and ln$Z$ *vs.* ln[sinh($\alpha\sigma$)] (c) obtained from the flow curves at a true strain of 0.8.

Table 1
Comparison of activation energy for hot deformation (Q) for some intermetallic phases of iron aluminides.

Alloy (at.%)	Deformation conditions (temperature/ strain rate)	Activation energy, Q	Remarks	Ref.
Fe–25Al-1.5Ta	800–850 °C/ 0.0013–0.1 s^{-1}	540 kJ mol^{-1}	Spark plasma sintered, deformed in B2-region	Present study
Fe–25Al-1.5Ta	900–1100 °C/ 0.0013–0.1 s^{-1}	385 kJ mol^{-1}	As-cast, deformed in A2-region	[35]
		436 kJ mol^{-1}	Spark plasma sintered, deformed in A2-region	[11]
		344 kJ mol^{-1}	Laser powder bed fused, deformed in A2-region	[36]
Fe–16Al–5Cr–1Mo-0.1Zr	600–1100 °C/ 0.001–100 s^{-1}	200 kJ mol^{-1}	Cast and homogenized	[21]
Fe-28.7Al-2.5Cr	700–1050 °C/ 0.001–10 s^{-1}	340 kJ mol^{-1}	Cast and homogenized	[18,37]
Fe-27.6Al	750–1050 °C/ 0.001–10 s^{-1}	260 kJ mol^{-1}	Cast and homogenized	[18]
Fe–26Al	800–1000 °C/ 5–20 s^{-1}	700 kJ mol^{-1}	As-cast, deformed in B2-region	[38]
		300 kJ mol^{-1}	As-cast, deformed in A2-region	

•αFe (A2), disordered bcc
•FeAl (B2), ordered bcc

all deformed specimens is characterized by flat, heavily deformed grains elongated perpendicular to the compression axis (CA). A few substructures are visible inside the deformed grains, e.g., Grain A (marked by red letters in Fig. 7(a)), which may indicate dislocation recovery and reorientation into subgrains. In addition to the substructures within the deformed grains, some small equiaxed grains are observed near the initial grain boundaries. The small grains are more pronounced in the specimens deformed at the higher strain rate of 1 s^{-1}, as can be seen in (b), (d), and (f). A representative example of such a deformed grain is illustrated in Fig. 8, where the grain boundary region is marked by a red line. The deformed grain is fragmented into subregions with a variation in BSE contrast. Some exemplary substructures inside the grain are marked by white lines. Some small grains in regions close to grain boundaries show a different crystal orientation contrast than the substructured regions. These grains result from recrystallization during hot deformation, which will be discussed later using EBSD results.

It is worth noting that the recrystallization does not coincide in different deformed grains, and the grain size distribution is inhomogeneous. This behavior is due to the anisotropy of the mechanical properties of the Fe_3Al-based alloys, which leads to inhomogeneous plastic deformation and orientation-dependent recrystallization [22].

In the following sections, the correlation between the microstructure of the deformed specimens and the corresponding processing windows will be discussed.

4.1. *Flow softening mechanisms*

The evolution of the microstructure and the underlying deformation mechanisms involved in the deformation regions of D1 and D2 in the processing map are discussed below:

- D1: 840–850 °C/0.0013–0.005 s^{-1} – A stable flow region with the highest efficiency where the power dissipation efficiency ranges from 35% to 45%. At 850 °C/0.0013 s^{-1}, the highest power dissipation efficiency ($\eta \approx 45\%$) and strain rate sensitivity ($m = 0.29$) are reached. Fig. 9 exhibits EBSD inverse pole figure (IPF) maps and a phase map overlaid with a GB misorientation map for the sample deformed at 850 °C/0.0013 s^{-1}. The deformed grains are fragmented into subregions with a continuous variation of colors in the IPF maps, indicating the annihilation of dislocations and their rearrangement into substructures (DRV). Some substructures have already evolved into subgrains bounded by LAGBs, as marked by white lines in Fig. 9 (a), which could serve as a pre-requisite for initiating continuous DRX as deformation proceeds. In addition to the substructures, some

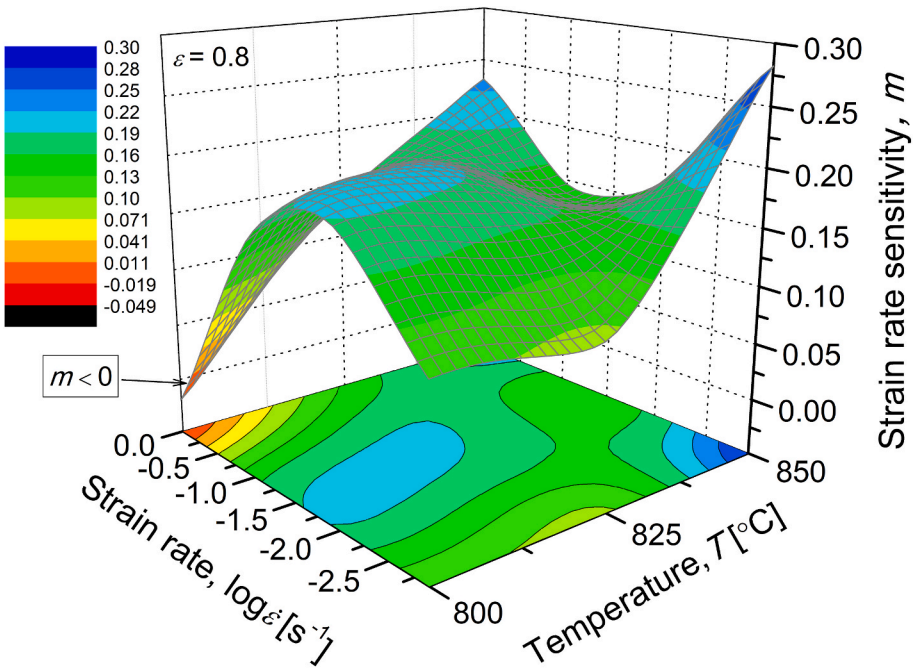

Fig. 5. 3D strain rate sensitivity, *m*, map for the Fe–25Al-1.5Ta alloy at a true strain of 0.8. The region of negative *m* values is indicated by an arrow.

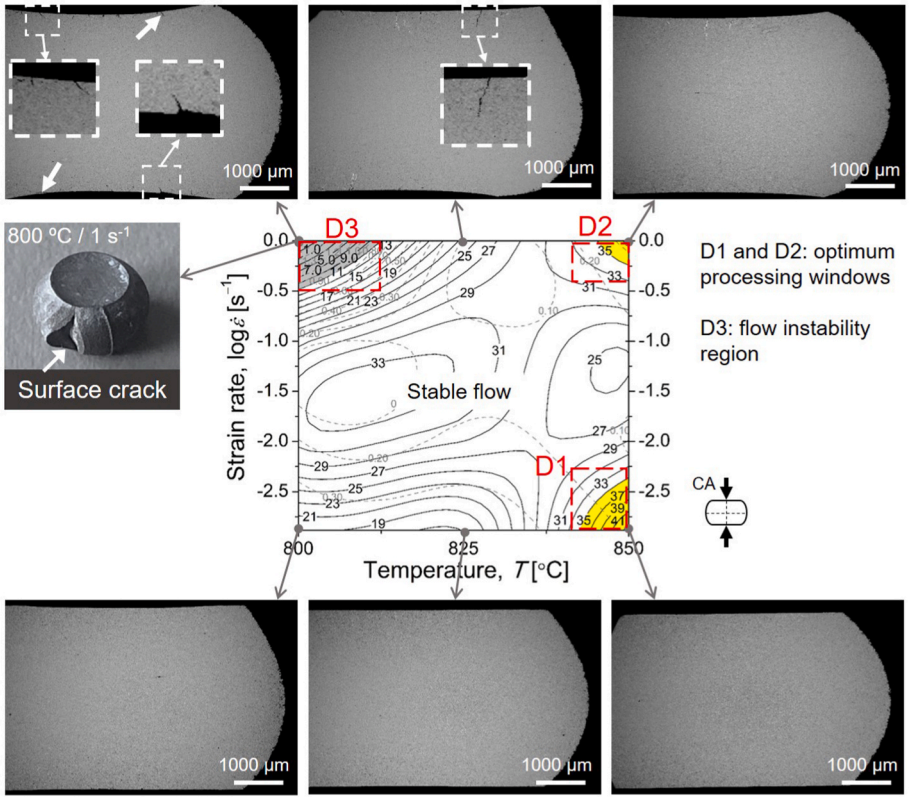

Fig. 6. Processing map for the Fe–25Al-1.5Ta alloy at a true strain of 0.8 showing stable flow regions (denoted as D1 and D2) with an efficiency higher than 33%. The shaded region D3 represents a low-efficiency region, including flow instability at 800 °C/1 s^{-1} resulting from $m < 0$. The areas highlighted in yellow illustrate the optimum processing windows with the most efficient energy dissipation. The solid and dash contour numbers indicate the efficiency of power dissipation in percent and the instability parameter, respectively. Insets show the BSE-SEM micrographs for the samples deformed in each region. The specimen deformed at 800 °C/1 s^{-1} shows a longitudinal crack expanding through the surface. The specimens deformed with a higher strain rate of 1 s^{-1} between 800 °C and 825 °C exhibit micro-cracks (marked by squares) originating from the surfaces in contact with the deformation punches. The compression axis (CA) is vertical.

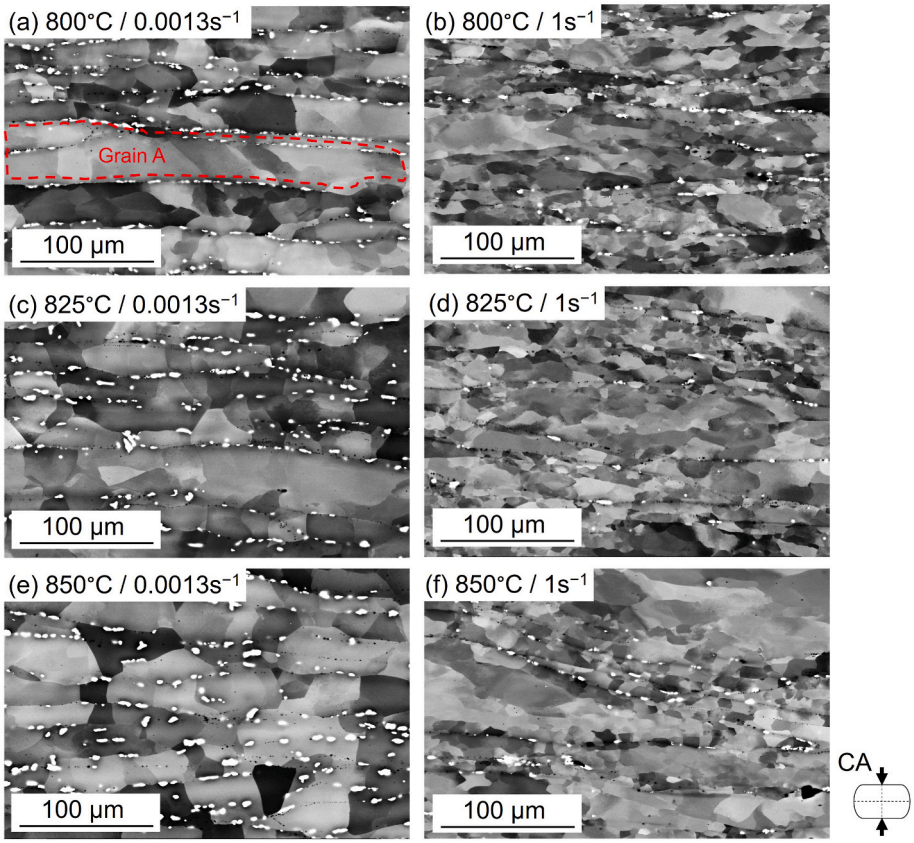

Fig. 7. Representative BSE-SEM micrographs for the Fe–25Al-1.5Ta specimens hot compressed to a true strain of 0.8 at different deformation conditions showing elongated deformed grains with substructures inside (e.g., Grain A) and a few small grains located close to the original grain boundary regions. The C14 Laves phase precipitates appear white in the micrographs. The compression axis (CA) is vertical.

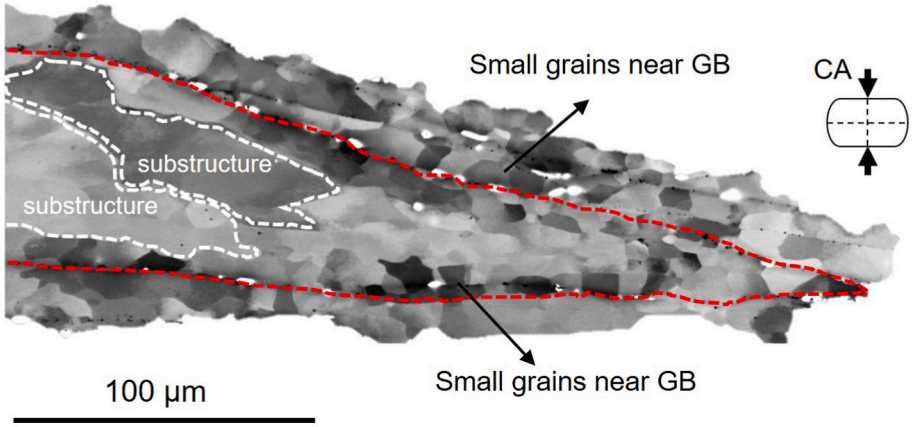

Fig. 8. Enlargement of a typical deformed grain in the sample compressed at 850 °C/1 s^{-1} to a true strain of 0.8, showing substructures inside the grain and small equiaxed grains close to the original grain boundaries (GB). Red and white lines mark grain boundaries and some exemplary substructures within the grain, respectively. The compression axis (CA) is vertical.

small equiaxed grains are visible near initial grain boundaries, indicated by circles in Fig. 9(b). These equiaxed, fine grains are surrounded by black-colored HAGBs, and therefore, they can be identified as recrystallized grains formed near pre-existing grain boundaries during deformation.

- D2: 840–850 °C/0.4–1 s^{-1} – A stable flow region with lower power dissipation efficiency between 33% and 38% is located in areas with significantly higher strain rates compared to D1. Similar to D1, the microstructural features suggest a combination of DRV and DRX as the dominant deformation mechanisms in this region (see Fig. 7(f)).

4.2. Flow instability mechanism

- D3: 800–812 °C/0.31–1 s^{-1} – The flow region with the lowest efficiency of less than 10% is located at lower temperatures and higher strain rates. This area corresponds to the region with the lowest m values (see Fig. 5), including a negative value of −0.027 at 800 °C/1 s^{-1}, indicating that damage mechanism(s) occurred during deformation. The microstructures of the specimens deformed in this domain exhibit micro-cracks originating from the surfaces in contact with the deformation punches (indicated by squares in Fig. 6). In

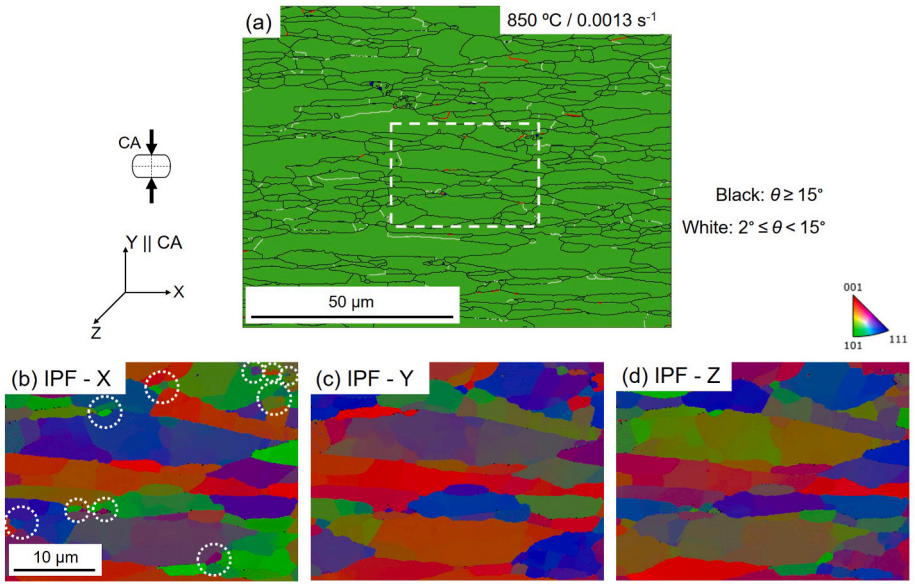

Fig. 9. EBSD phase map overlaid with GB misorientation map (a) and inverse pole figure (IPF) maps (b) for the Fe–25Al-1.5Ta specimen compressed at 850 °C/0.0013 s^{-1} (corresponding to D1 in the processing map) showing substructures within the deformed grains and small recrystallized grains near the initial grain boundaries (marked by circles). The black and white lines in (a) mark low-angle grain boundaries with misorientations (θ), $2° \leq \theta < 15°$ and high-angle grain boundaries with $\theta \geq 15°$, respectively. The IPF maps in (b) to (d) show high-resolution views of the region outlined a square in (a). The compression axis (CA) is vertical.

addition, the specimen compressed at 800 °C/1 s^{-1} shows a macro-crack in the longitudinal direction expanding over the entire surface. Therefore, deformation processing in the D3 domain should be avoided due to the significantly lower power dissipation efficiency (less than 10%) and the low deformability due to the cracks.

4.3. The effect of laves phase precipitates on recovery and recrystallization behaviors

The following section discusses the potential role of the C14-(Fe, Al)$_2$Ta Laves phase precipitates, which decorate the original grain boundaries, in recovery and recrystallization behaviors during hot deformation. It is well known that the second phase precipitates can impede dislocation movement, resulting in a slower rate of recovery. Nevertheless, they can promote recrystallization by particle-stimulated nucleation (PSN) mechanism [39]. A recent study by the authors has investigated the DRX mechanism in Fe–25Al-1.5Ta cast alloy at the boundaries containing large Laves phase particles [43]. It was found that some recrystallized grains were located around Laves phase particles close to the grain boundary regions containing a cluster of large particles. Coarse Laves phase particles are likely to induce heterogeneous deformation and a high degree of local lattice curvature in their vicinity due to the strain incompatibility between particles and matrix. As a result, deformation zones, including complex dislocation structures, are formed around the particles. During hot deformation, such particle-related deformation zones are favorable nucleation sites for recrystallizing grains. In contrast, the dominant DRX mechanism at the particle-free boundaries was strain-induced bulging of original grain boundaries.

5. Conclusions

The hot deformation behavior and microstructural evolution of an Fe–25Al-1.5Ta alloy produced by spark plasma sintering were investigated using hot-compression tests with strain rates from 0.0013 s^{-1} to 1 s^{-1} at temperatures between 800 and 850 °C, where the ordered B2–FeAl and the C14-(Fe, Al)$_2$Ta Laves phase coexisted. Based on the flow stress-strain behaviors and microstructural observations, the main conclusions can be summarized as follows:

1. The flow stress-strain curves for the specimens deformed at a strain rate of less than 1 s^{-1} showed a broad maximum followed by a slight decrease until a steady state was reached. When deformed at a strain rate of 1 s^{-1}, the flow curves exhibited a distinct stress peak followed by a stress drop.
2. The constitutive equation for hot deformation for the studied Fe–25Al-1.5Ta alloy can be formulated as: $\sigma = \frac{1}{0.005} ln\left[\left(\frac{Z}{2.8\times10^{32}}\right)^{1/4.87} + \left(\left(\frac{Z}{2.8\times10^{32}}\right)^{2/4.87} + 1\right)^{1/2}\right]$.
3. The activation energy (Q) for hot deformation was averaged to 540 kJ mol^{-1} over the entire deformation range in the (B2 + C14)-phase field using the stress-strain data obtained from the flow curves.
4. The optimum processing window for the studied alloy was located at 850 °C/0.0013 s^{-1}, where the power dissipation efficiency (η) and strain rate sensitivity (m) reached 50% and 0.25, respectively.
5. The processing map predicted a domain of flow instability, resulting from cracking, in the range of lower temperatures and higher strain rates (800 °C/1 s^{-1}).
6. The dynamic recovery of the dislocations into substructures and the formation of fine recrystallized grains at the pre-existing grain boundaries were characterized as possible mechanisms of flow softening.

From the point of view of cost-efficiency in forging, lower processing temperatures are always preferable. In this context, the current study shows a well-suited parameter range to achieve a high degree of hot deformability in Fe–Al alloys at significantly lower temperatures than those commonly used. This can contribute to a reduction in energy consumption in industrial forging operations.

Author contributions

A. Emdadi: Conceptualization, Methodology, Investigation, Writing-original draft preparation, Writing-Review & Editing, Supervision. M. Tovar: Investigation. A. Jedynak: Investigation. S. Weiß: Writing-Review

& Editing. All authors have read and agreed to the published version of the manuscript.

Funding

This research did not receive any specific grant from funding agencies in the public, commercial, or not-for-profit sectors.

Declaration of competing interest

The authors declare that they have no known competing financial interests or personal relationships that could have appeared to influence the work reported in this paper.

Data availability

Data will be made available on request.

Acknowledgments

The material and process development was supported by the Graduate Research School “LokPro” at BTU Cottbus-Senftenberg. A. Emdadi acknowledges Access e.V. Center (Aachen, Germany) for the help with electron microscopy.

References

[1] M. Palm, F. Stein, G. Dehm, Iron aluminides, Annu. Rev. Mater. Res. 49 (2019) 297–326, https://doi.org/10.1146/annurev-matsci-070218-125911.
[2] D.G. Morris, M.A. Muñoz-Morris, Recent developments toward the application of iron aluminides in fossil fuel technologies, Adv. Eng. Mater. 13 (2011) 43–47, https://doi.org/10.1002/adem.201000210.
[3] D.D. Risanti, G. Sauthoff, Microstructures and mechanical properties of Fe–Al–Ta alloys with strengthening Laves phase, Intermetallics 19 (2011) 1727–1736, https://doi.org/10.1016/j.intermet.2011.07.008.
[4] P. Prokopčáková, M. Švec, M. Palm, Microstructural evolution and creep of Fe–Al–Ta alloys, IJMR 107 (2016) 396–405, https://doi.org/10.3139/146.111357.
[5] M. Palm, Fe–Al materials for structural applications at high temperatures: current research at MPIE, IJMR 100 (2009) 277–287, https://doi.org/10.3139/146.110056.
[6] P. Hanus, E. Bartsch, M. Palm, R. Krein, K. Bauer-Partenheimer, P. Janschek, Mechanical properties of a forged Fe–25Al–2Ta steam turbine blade, Intermetallics 18 (2010) 1379–1384, https://doi.org/10.1016/j.intermet.2009.12.035.
[7] A. Hotař, M. Palm, Oxidation resistance of Fe–25Al–2Ta (at.%) in air, Intermetallics 18 (2010) 1390–1395, https://doi.org/10.1016/j.intermet.2010.02.014.
[8] F. Stein, A. Schneider, G. Frommeyer, Flow stress anomaly and order–disorder transitions in Fe3Al-based Fe–Al–Ti–X alloys with X=V, Cr, Nb, or Mo, Intermetallics 11 (2003) 71–82, https://doi.org/10.1016/S0966-9795(02)00187-5.
[9] V.T. Witusiewicz, A.A. Bondar, U. Hecht, V.M. Voblikov, N.I. Tsyganenko, O. S. Fomichov, M.V. Karpets, V.M. Petyukh, T.Y. Velikanova, Experimental study and thermodynamic modelling of the ternary Al–Fe–Ta system, J. Mater. Sci. 48 (2013) 377–412, https://doi.org/10.1007/s10853-012-6755-x.
[10] A. Emdadi, High-Temperature Deformation Behavior of Intermetallic Titanium and Iron Aluminides Produced by Spark Plasma Sintering, first. Auflage, Shaker, Düren, 2021.
[11] A. Emdadi, I. Sizova, M. Bambach, U. Hecht, Hot deformation behavior of a spark plasma sintered Fe-25Al-1.5Ta alloy with strengthening Laves phase, Intermetallics 109 (2019) 123–134, https://doi.org/10.1016/j.intermet.2019.03.017.
[12] V.T. Witusiewicz, A.A. Bondar, U. Hecht, V.M. Voblikov, O.S. Fomichov, V. M. Petyukh, S. Rex, Experimental study and thermodynamic re-assessment of the binary Fe–Ta system, Intermetallics 19 (2011) 1059–1075, https://doi.org/10.1016/j.intermet.2011.03.018.
[13] A. Emdadi, I. Sizova, O. Stryzhyboroda, U. Hecht, J. Buhl, M. Bambach, Hot workability of a spark plasma sintered intermetallic iron aluminide alloy above and below the order-disorder transition temperature, Procedia Manuf. 47 (2020) 1281–1287, https://doi.org/10.1016/j.promfg.2020.04.238.
[14] A. Emdadi, S. Weiß, A comparative study of microstructure and hot deformability of a Fe–Al–Ta iron aluminide prepared via additive manufacturing and conventional casting, Crystals 12 (2022) 1709, https://doi.org/10.3390/cryst12121709.
[15] A. Emdadi, S. Bolz, F. Jensch, M. Tovar, S. Weiß, On the hot deformation of a Fe-Al-Ta iron aluminide prepared via laser powder bed fusion, Crystals 13 (2023) 627, https://doi.org/10.3390/cryst13040627.
[16] A. Emdadi, S. Bolz, J. Buhl, S. Weiß, M. Bambach, Laser powder bed fusion additive manufacturing of Fe3Al-1.5Ta iron aluminide with strengthening Laves phase, Metals 12 (2022) 997, https://doi.org/10.3390/met12060997.
[17] B. Voyzelle, J.D. Boyd, High-temperature deformation behaviour of Fe3Al, Mater. Sci. Eng., A 258 (1998) 243–248, https://doi.org/10.1016/S0921-5093(98)00940-X.
[18] R.S. Sundar, R.G. Baligidad, Y.V.R.K. Prasad, D.H. Sastry, Processing of iron aluminides, Mater. Sci. Eng., A 258 (1998) 219–228, https://doi.org/10.1016/S0921-5093(98)00937-X.
[19] R. Łyszkowski, J. Bystrzycki, T. Płociński, Processing maps for hot working of FeAl-based alloy, Intermetallics 18 (2010) 1344–1347, https://doi.org/10.1016/j.intermet.2009.12.026.
[20] R. Łyszkowski, J. Bystrzycki, Hot deformation and processing maps of an Fe3Al intermetallic alloy, Intermetallics 14 (2006) 1231–1237, https://doi.org/10.1016/j.intermet.2005.12.014.
[21] R. Łyszkowski, J. Bystrzycki, Hot deformation and processing maps of a Fe–Al intermetallic alloy, Mater. Char. 96 (2014) 196–205, https://doi.org/10.1016/j.matchar.2014.07.004.
[22] Y.D. Huang, L. Froyen, Recovery, recrystallization and grain growth in Fe3Al-based alloys, Intermetallics 10 (2002) 473–484, https://doi.org/10.1016/S0966-9795(02)00019-5.
[23] I.S. Golovin, A. Emdadi, A.M. Balagurov, I.A. Bobrikov, J. Cifre, M.Y. Zadorozhnyy, A. Rivière, Anelasticity of iron-aluminide Fe 3 Al type single and polycrystals, J. Alloys Compd. 746 (2018) 660–669, https://doi.org/10.1016/j.jallcom.2018.02.336.
[24] Y.D. Huang, W.Y. Yang, G.L. Chen, Z.Q. Sun, On the effect of the B2 thermomechanical treatment in improving the room temperature ductility of Fe3Al-based alloys, Intermetallics 9 (2001) 331–340, https://doi.org/10.1016/S0966-9795(01)00007-3.
[25] S. Divinski, Defects and diffusion in ordered compounds, in: Handbook of Solid State Diffusion, ume 1, Elsevier, 2017, pp. 449–517.
[26] Peng Moszner, Jasnau Suutala, Palm Damani, Application of iron aluminides in the combustion chamber of large bore 2-stroke marine engines, Metals 9 (2019) 847, https://doi.org/10.3390/met9080847.
[27] Y.V.R.K. Prasad, H.L. Gegel, S.M. Doraivelu, J.C. Malas, J.T. Morgan, K.A. Lark, D. R. Barker, Modeling of dynamic material behavior in hot deformation: forging of Ti-6242, MTA 15 (1984) 1883–1892, https://doi.org/10.1007/BF02664902.
[28] Y.V.R.K. Prasad, T. Seshacharyulu, Modelling of hot deformation for microstructural control, Int. Mater. Rev. 43 (1998) 243–258, https://doi.org/10.1179/imr.1998.43.6.243.
[29] Y.V.R.K. Prasad, Processing maps: a status report, J. Mater. Eng. Perform. 12 (2003) 638–645, https://doi.org/10.1361/105994903322692420.
[30] H. Ziegler, Eidgenössische Technische Hochschule., Some Extremum Principles in Irreversible Thermodynamics, with Application to Continuum Mechanics, 1962.
[31] K. Huang, R.E. Logé, A review of dynamic recrystallization phenomena in metallic materials, Mater. Des. 111 (2016) 548–574, https://doi.org/10.1016/j.matdes.2016.09.012.
[32] N. Tsuji, Y. Matsubara, Y. Saito, Dynamic recrystallization of ferrite in interstitial free steel, Scripta Mater. 37 (1997) 477–484, https://doi.org/10.1016/S1359-6462(97)00123-1.
[33] N. Tsuji, Y. Matsubara, Y. Saito, T. Maki, Occurrence of dynamic recrystallization in ferritic iron, J. Jpn. Inst. Metal. 62 (1998) 967–976, https://doi.org/10.2320/jinstmet1952.62.10_967.
[34] C.M. Sellars, W.J. McTegart, On the mechanism of hot deformation, Acta Metall. 14 (1966) 1136–1138, https://doi.org/10.1016/0001-6160(66)90207-0.
[35] A. Emdadi, H. Michels, M. Tovar, Hot workability investigation of an Fe-Al-Ta alloy using deformation processing maps, Metals 13 (2023) 1195, https://doi.org/10.3390/met13071195.
[36] A. Emdadi, S. Bolz, S. Weiß, Hot working of an Fe-25Al-1.5Ta alloy produced by laser powder bed fusion, Crystals 13 (2023) 1335, https://doi.org/10.3390/cryst13091335.
[37] R.S. Sundar, D.H. Sastry, Y.V.R.K. Prasad, Hot workability of as-cast Fe3Al–2.5%Cr intermetallic alloy, Mater. Sci. Eng., A 347 (2003) 86–92, https://doi.org/10.1016/S0921-5093(02)00585-3.
[38] J. Konrad, S. Zaefferer, A. Schneider, D. Raabe, G. Frommeyer, Hot deformation behavior of a Fe3Al-binary alloy in the A2 and B2-order regimes, Intermetallics 13 (2005) 1304–1312, https://doi.org/10.1016/j.intermet.2004.10.017.
[39] A.D. Rollett, G.S. Rohrer, J. Humphreys, Recrystallization and Related Annealing Phenomena, third ed., Anthony Rollett, Gregory S. Rohrer, Elsevier, Amsterdam, 2017.
[40] A. Emdadi, O. Stryzhyboroda, U. Hecht, M. Bambach, Complex dynamic restoration processes leading to a high degree of deformability in a dual-phase Al0.5CoCrFeNi high entropy alloy, J. Alloys Compd. 918 (2022), 165583, https://doi.org/10.1016/j.jallcom.2022.165583.
[41] T. Bhattacharjee, I.S. Wani, S. Sheikh, I.T. Clark, T. Okawa, S. Guo, P. P. Bhattacharjee, N. Tsuji, Simultaneous strength-ductility enhancement of a nano-lamellar AlCoCrFeNi2.1 eutectic high entropy alloy by cryo-rolling and annealing, Sci. Rep. 8 (2018) 3276, https://doi.org/10.1038/s41598%2D018%2D21385%2Dy.
[42] P. Shi, W. Ren, T. Zheng, Z. Ren, X. Hou, J. Peng, P. Hu, Y. Gao, Y. Zhong, P. K. Liaw, Enhanced strength-ductility synergy in ultrafine-grained eutectic high-entropy alloys by inheriting microstructural lamellae, Nat. Commun. 10 (2019) 489, https://doi.org/10.1038/s41467-019-08460-2.
[43] A. Emdadi, Y. Yang, S. Bolz, O. Stryzhyboroda, M. Tovar, S. Gein, U. Hecht, S. Weiß, Mechanisms of necklace recrystallization in a BCC Fe-Al-Ta alloy with strengthening Laves phase precipitates, Scripta Mater. 237 (2023), 115705, https://doi.org/10.1016/j.scriptamat.2023.115705.